

Double helical plasmonic antennas

Aleksei Tsarapkin,^{1,*} Luka Zurak,² Krzysztof Maćkosz,³ Ivo Utke,³ Thorsten Feichtner,² and Katja Höflisch^{1,†}

¹*Ferdinand-Braun-Institut (FBH), Gustav-Kirchhoff-Str. 4, D-12489 Berlin, Germany*

²*Experimental Physics 5, University of Würzburg, Am Hubland, D-97074 Würzburg, Germany*

³*Laboratory for Mechanics of Materials and Nanostructures,
Empa – Swiss Federal Laboratories for Materials Science and Technology,
Feuerwerkerstrasse 39, CH-3602 Thun, Switzerland*

(Dated: July 23, 2024)

Plasmonic double helical antennas are a means to funnel circularly polarized states of light down to the nanoscale. Here, an existing design tool for single helices is extended to the case of double helices and used to design antennas that combine large chiroptical interaction strength with highly directional light emission. Full-field numerical modeling underpins the design and provides additional insight into surface charge distributions and resonance widths. The experimentally realized double helical antennas were studied regarding their polarization-dependent transmission behavior resulting in a large and broadband dissymmetry factor in the visible range. Since the polarization of light is an important tool for implementing logic functionality in photonic and quantum photonic devices, these helices are potential building blocks for future nanophotonic circuits, but also for chiral metamaterials or phase plates.

Keywords: Plasmonics, Helical Antenna, Focused Electron-Beam Induced Deposition

I. INTRODUCTION

The enhancement of light-matter interaction and the coherent manipulation of light at the nanoscale are major goals of photonic quantum technology, to enable the transition from bulky laboratory setups to miniaturized on-chip devices [1]. This requires the integration of quantum functionalities onto photonic chips, i.e. solid-state based qubits strongly coupled to a single optical mode populated with photons carrying the quantum information. According to Purcell's formula [2], there are two fundamentally different approaches to enhance light-matter interaction, both of which have their own advantages and shortcomings. Either the interaction time can be increased by minimizing losses in resonators, leading to extremely large quality factors Q [3], or the interaction probability can be increased by reducing the mode volume V through resonant polariton-based near-field interactions in open cavities or antenna systems [4, 5]. The latter can be based on surface plasmon polaritons in metals arising from the collective motion of free electrons coupled to visible light [6] or other polaritonic material resonances such as exciton or phonon polaritons [7]. Especially resonant plasmonic antennas allow to combine extremely high emitter decay rates due to a small mode volume with a relatively broadband operation due to their moderate Q factor [5]. These antennas can be further designed to couple to specific radiating modes [8] to e.g. achieve directional emission of quantum emitters [9]. In addition, chiral plasmonic components enable strongly enhanced chiroptical interactions [10–12] to tailor the circular polarization state of the emitted light in a com-

pact manner. Since polarization encoding is one of the most popular methods used in photonic quantum protocols [13], the realization of such nanoscale components that improve quantum emission and additionally provide directional and polarization control is in high demand.

In RF-technology, direct access to (far-field) circular polarization is realized by helical antennas [14]. A plasmonic single turn helix – substantially smaller than the wavelength of light – can be regarded as a nearly perfect chiral dipole for its fundamental resonance [15]. Making use of all supported mode orders plasmonic helices with one or more turns can be designed for resonating in a specific wavelength range and emitting with high directivity [16, 17]. First attempts of co-integration have been successful, e.g. single helices were coupled to a dipole source realized as a slit at the bottom [18] and efficient coupling to surface-plasmon-polariton modes has been shown for the telecom wavelength regime [19]. In both cases, also highly directional circularly polarized light emission was observed.

Here, we go a step further by designing and fabricating double helical antennas that work in the visible to telecom regime. The two nano-wires couple, resulting in a hybridization of their plasmonic modes [20] [21] to both symmetric (dipole-forbidden) and antisymmetric (dipole-allowed) modes [22]. The antisymmetric mode concentrates the fields between the wires which allows both an enhanced coupling to dipolar quantum emitters placed in the gap and efficient interaction with circular polarized far-field radiation [17]. This concept has the potential to realize solid-state ultrabright spin-selective single-photon sources.

Based on our established understanding of the excitation mechanisms in a single helix, we extended a semi-analytical design tool [17] to describe double helices. Full-field electromagnetic modeling refines the pre-selected design and provides insight to the antisymmet-

* aleksei.tsarapkin@fbh-berlin.de

† katja.hoeflisch@fbh-berlin.de; <https://www.fbh-berlin.de/en/pqt>

ric mode patterns. For our chosen design the wavelength range below 1000 nm shows a chiroptical cross section almost twice as strong as for the single helical counterpart. Then the helices are fabricated via direct electron beam writing using Au(acac)Me₂ as precursor and a subsequent oxygen plasma treatment to obtain a pure gold shell. Finally, the fabricated antennas are optically characterized with respect to their circular dichroism.

II. RESULTS AND DISCUSSION

A. Theoretical Model

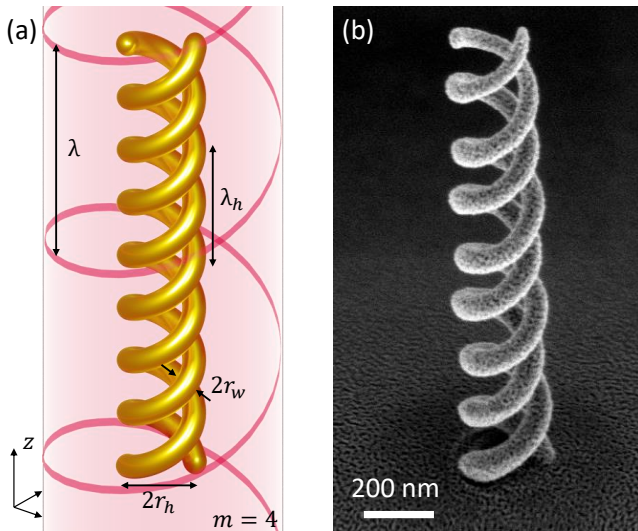


FIG. 1. (a) Geometry of a helical plasmonic antenna. A double plasmonic helix of $m = 4$ turns, helix radius $r_h = 100$ nm, helix pitch $\lambda_h = 430$ nm and wire radius $r_w = 32$ nm is illuminated by circularly polarized light propagating along the helix axis z . (b) SE micrograph of the double helix, deposited onto it on glass sample and purified in the oxygen plasma.

Figure 1(a) shows an artistic sketch of the studied system next to a scanning electron micrograph of a helix as realized in the experiment in panel (b). A double helix oriented along the z -axis is illuminated with a plane wave defined by a k -vector $k = 2\pi/\lambda$ pointing in the negative z direction. The right or left circular polarization (RCP and LCP) state is defined according to the book of Hecht [23]. We can understand the power coupled from the wave to the helix modes based on the theoretical description for single helices as introduced in [16]. The energy of the plane wave is given by $E = \hbar\omega = hc/\lambda = h\nu$ with the Planck constant h and the vacuum speed of light c . The helix geometry is defined by the helix radius r_h , the pitch height λ_h and the number of pitches m . The two wires are coiled into a double helix, separated by $2r_h$ and have a circular cross section with radius r_w . On each of these helix wires Fabry-Perot modes of order n can be excited [24]. The corresponding effective wave-

length of these plasmonic Fabry-Perot modes λ_{eff} can be calculated according to [24] using the material parameters for a Drude model of gold. Here, straight cylindrical wires of radius $r_w \ll \lambda$ are assumed which has been proven as suitable approximation for wires curved in such a way that the helix wire are sufficiently separated to avoid near-field coupling [16]. Finally, the power transfer from plane wave to helix mode can be treated as a one-dimensional integral along the helix axis [16, 17].

In the case of a double helix the modes will interact and hybridise (as depicted in Figure 2a), depending on their distance $d = 2r_h$, more exactly on their distance to wavelength ratio $d/\lambda_{\text{eff}} \propto k_{\text{eff}} \cdot d$ with $k_{\text{eff}} = 2\pi/\lambda_{\text{eff}}$ being the wire plasmon k -vector. Using the equations developed in [22] which simplify for two cylindrical wires with identical radius, the two frequencies of the hybridised modes can be calculated as:

$$\omega_{\pm}^2(k_{\text{eff}}) = \omega^2 \pm \sqrt{\omega^2 + \Delta} \quad (1)$$

$$\text{with } \Delta = [\omega^2 K_0(k_{\text{eff}} d)]^2 \frac{I_0(k_{\text{eff}} r_w)^2}{K_0(k_{\text{eff}} r_w)^2}, \quad (2)$$

where ω is the single wire plasmon frequency and K_0 and I_0 are the cylindrical Bessel functions used to describe the single wire mode field distribution. Keep in mind that both of these frequencies will lead to the same effective plasmon wavelength λ_{eff} , but for different hybridized modes (see Figure 2(b)): (i) The anti-symmetric mode with a positive charge opposed by a negative charge attracting each other over the gap leads to a decrease in the plasmon frequency and a red shift of the corresponding free space wavelength. (ii) The symmetric mode where the coupling charge maxima are of equal sign and repel each other leads to an increase of the plasmon frequency.

Figure 2(a) also explains why for a plane wave impinging along the z -axis only the anti-symmetric mode is observed. The symmetric mode leads to no dipole moments perpendicular to the helix axis. Therefore, from now on we only consider ω_- , which leads to a red shift of the modes at the transition from a single helix to a double helix. The wire distance d in (2) is the distance between the charge density maxima of the standing wave. For the helix geometry this is identical to its diameter $d = 2r_h$.

With the double helix plasmon frequency ω_- calculated via (1) both mode currents and overlap integral with the free space wavelength λ can be calculated [16, 17]. Thereby, the coupling strength is doubled since the integration of the mode overlap must be carried out for both wires. An updated version of the one-dimensional modeling tool can be found online[25].

B. Full-Field Modeling

Full-field electrodynamic modeling was used to study position and width of the resonant modes of the double

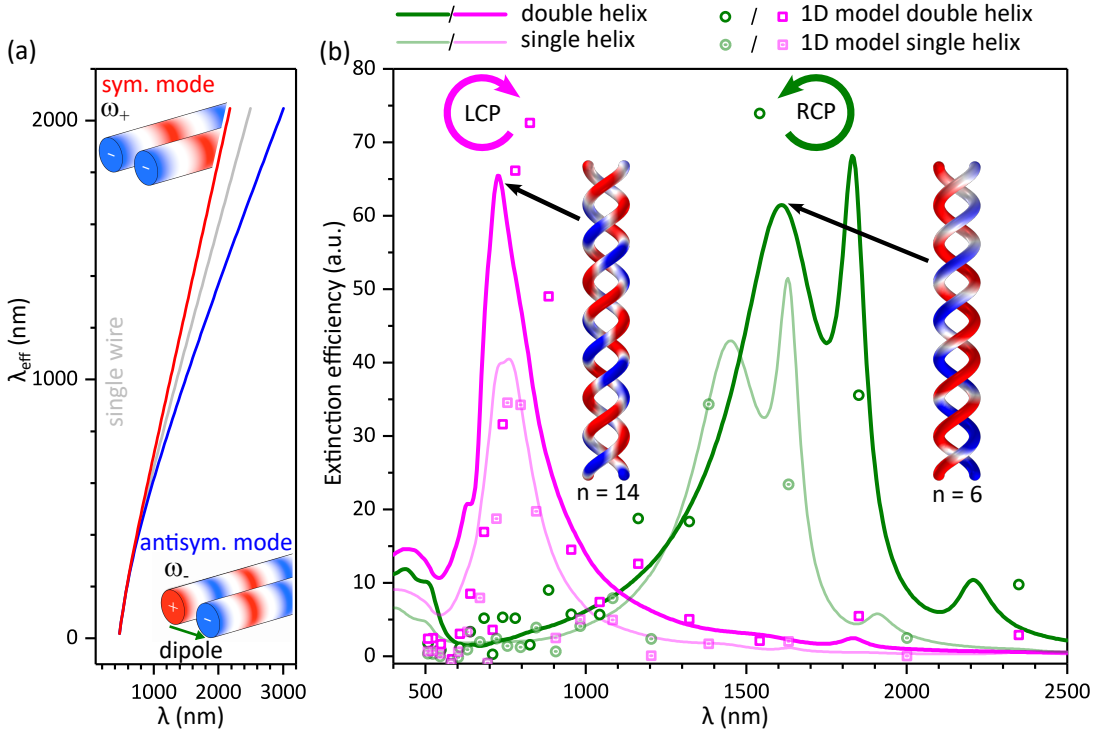


FIG. 2. (a) Dispersion relations for both single and double straight wires showing the mode splitting due to the coupling of the plasmonic modes (using eq. (1)). Insets visualize the symmetric and anti-symmetric coupling of the opposing wires. (b) Comparison of extinction efficiencies of free-standing single and double helices, when excited with RCP and LCP. Subplots with normalized surface charge distribution of a high ($n = 14$) and a low order ($n = 6$) modes in the double helix show an antisymmetric pattern. Points represent position and power, coupled to the plasmonic modes according to the 1D theoretical model.

helix. We characterize the spectral response by the extinction cross-section, with the extinguished light as the sum of scattering and absorption, normalized to the incident light intensity and the geometric cross section of the helix projected on the plane of incidence [26]. Figure 2(c) depicts the obtained spectra for a right-handed double helix with the material response of gold [27] under LCP (magenta) and RCP (dark green) plane wave incidence. The lighter colored graph is added for comparison with the corresponding single helix with identical geometry parameters and material response. The resonance positions and transferred powers obtained from the semi-analytical model are plotted for LCP (open circles) and RCP (open squares) in the same color scheme. Surface charge distributions from the full-field simulations of selected modes are depicted in the insets of Figure 2(c), with red/blue color indicating lack/excess of electrons. The mode order n is equal to the number of nodes of the fields inside the helix.

Overall, the observed spectral features of the double helix closely resemble those of the single helix. While in the low-energy region modes are efficiently excited for matching handedness of helix and incident light, in the high-energy region a strong response is obtained for opposite handedness [16]. In the wavelength range above 1100 nm the helix exhibits three distinct resonant modes

for the excitation with light of matching handedness. Compared to the single helix, all of these modes are stronger and red-shifted due to the expected near-field mediated coupling. This red-shift is well-described by the semi-analytical model, in which the resonance positions were calculated for the antisymmetric modes according to the dispersion relation in Figure 2(a).

The mode observed at lowest energy is excited by RCP light at 2205 nm. In this case the number of nodes ($n = 4$) in the corresponding standing wave pattern equals the number of helix turns ($m = 4$). While this mode is strongest for excitation with a localized dipole source in the near-field [17], the overlap condition with an external plane wave is non-optimal. This is different for the dominating modes with matching handedness of the orders $n = 5$ and $n = 6$, as the mode overlap with the incident electric field is substantially enlarged [16, 17, 24]. The resonance width of the $n = 5$ mode at a wavelength of 1830 nm is significantly reduced compared to the neighboring modes. This could potentially be interesting for an application as plasmonic cavity mode, as the reason for the reduced width is the decreased coupling to the far-field. In plasmonic antennas this implies that all energy that is not scattered into the far-field is instead dissipated within the metal as heat. Accordingly, the narrow $n = 5$ mode is absorption-dominated (cf. SI

Figure SI2). In contrast, the $n = 6$ mode at 1610 nm (in the telecom L-band) is strongly scattering and therefore well-suited for antenna applications in the telecom range. The inset depicts the corresponding standing wave pattern which is antisymmetric with respect to the opposing helix arms. As expected, no symmetric surface charge distributions are excited.

For decreasing free space wavelengths from 1000 to 500 nm the red-shift due to coupling converges to zero (cf. also eq. (2)), as the mode overlap between the wires scales with the effective plasmon wavelength. Between 600 and 900 nm a multitude of closely spaced higher order modes is efficiently excited which we refer to as high-energy mode complex in the following. The surface charge distribution for the spectral maximum at a wavelength at 725 nm resembles an antisymmetric mode of the order $n = 14$. In terms of possible applications, the far-field radiation properties of all excitable modes are important. Figure 3(a) depicts far-field radiation patterns for the discussed modes of orders $n = 5, 6$, and 14. Especially, the high-energy mode complex surrounding the $n = 14$ mode is exceptionally directional and in addition features low absorption (cf. SI Figure SI2). This offers potential applications for nonlinear light generation, where telecom light with one handedness is converted into visible light with the opposite handedness. In case of second harmonic generation (SHG), for example, incoming light with a wavelength of 1400 - 1600 nm is converted into light with a wavelength of 700 - 800 nm and efficiently re-radiated into the far field, as both bands feature highly efficient modes.

C. Experimental Realization

Double helices were fabricated by direct electron beam writing [28, 29] and purified using a room-temperature ozone plasma treatment [30]. Figure 1(b) depicts a scanning electron micrograph of a prototypical double helical antenna after the plasma purification. To cross-check the geometry-dependent sign-change for the respective circular dichroism, double helices of either handedness have been fabricated.

Confocal transmission spectroscopy was employed for the characterization of the optical response of the double helical antennas. The obtained transmittance spectra were used to calculate the dissymmetry factor:

$$g_{\text{exp}} = \frac{2(T_{\text{RCP}} - T_{\text{LCP}})}{2 - T_{\text{RCP}} - T_{\text{LCP}}} \quad (3)$$

and compared to the dissymmetry factor g_{num} obtained by numerical modeling (cf. Methods Section for more details). Figure 3(b) displays the experimentally obtained dissymmetry spectra in the range of 500 to 800 nm for left-handed (cyan) and right-handed (navy) double helices compared to the full-field modeling. When taking into account the residual gold around on the surface around

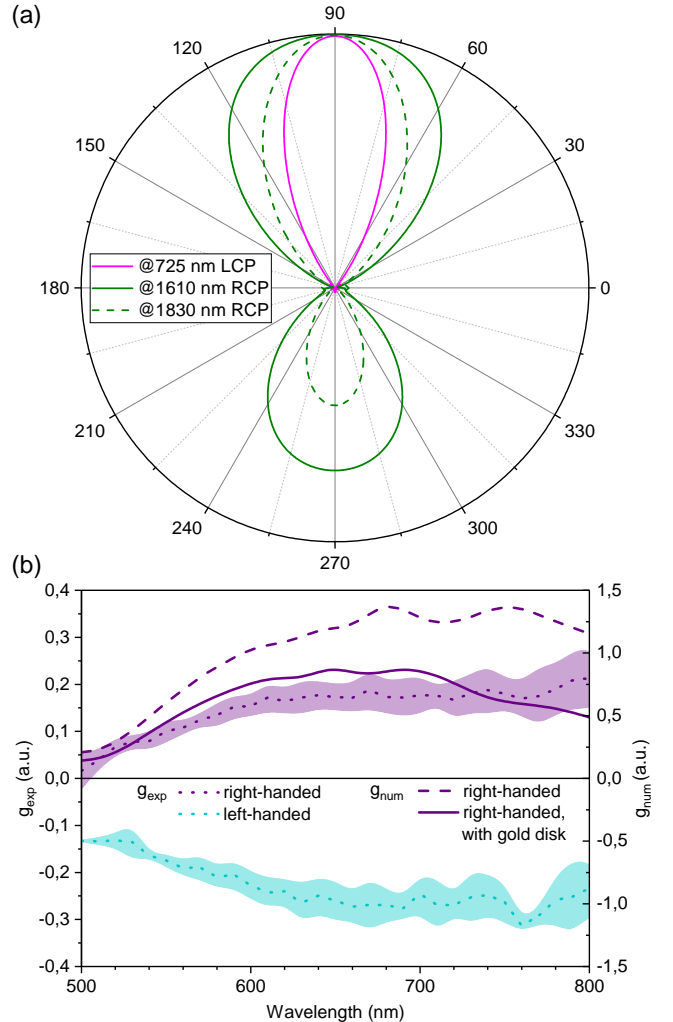


FIG. 3. Modeled far-field radiation and comparison of the far-field response between theory and experiment. (a) Normalized radiation pattern based on simulation results for scattering of the double helix at 725 nm LCP and 1610 and 1830 nm RCP in the far-field. (b) Comparison of the experimental dissymmetry factor g_{exp} with theoretical g_{num} obtained by full-field modeling of the transmission setup with the right-handed double helix on the substrate.

each helix, experiment and modeling show good agreement. In this wavelength range the individual modes of the high-energy mode complex cannot be spectrally resolved and instead only appear as slight modulation. Such a broadband operation with dissymmetry factors between 0.2 and 0.3 is interesting for the coupling to multicolor quantum emitters in the visible range [17, 31].

III. CONCLUSIONS

Here, plasmonic double helices acting as sensitive antennas for circularly polarized light were designed and experimentally demonstrated. Upon interaction with cir-

cularly left and right polarized light, modes with anti-symmetric surface charge distribution along the coupled wires are efficiently excited. The previously developed analytical tool for a single helix [16] was extended to account for the second helical arm by implementing mode coupling [22]. The designed helices were modeled using full-field finite element and finite-difference time-domain simulations to retrieve the width and surface charge distributions of their modes. The far-field radiation especially for the high-energy mode complex is highly directional. The experimental realization of the double helical antennas was carried out using direct electron beam writing followed by ozone plasma purification [30]. The fabricated double helices were characterized with respect to their transmission, revealing large circular dissymmetry factors in a broad wavelength range between 500 and 800 nm. Therewith, double helical antennas are a possible building block for chiral metamaterials or phase arrays[32, 33] with the prospect of two-dimensional chiroptical components for (color-sensitive) beam steering and focusing. In addition, the individual helical antennas can serve as a highly directional far-field receivers for chiral light to be concentrated below the diffraction limit and enable strong light-matter interaction at the nanoscale. The special design would even allow to implement a non-linear helicity switch in which the circularly polarized input light generates a second harmonic radiation with twice the energy and opposite circular polarization. Hence, in a broader sense, these results can form the basis for future developments in the fields of plasmonic circuitry and photonic quantum technology.

IV. METHODS

a. Numerical Modeling Full-field modeling was carried out using commercial Maxwell solvers. Two different modeling techniques were employed. The scenario without substrate corresponding to the described case in the semi-analytical model was modeled using the finite element method (FEM). The scenario with substrate was modeled using a finite-difference time-domain (FDTD) technique. While in FEM the triangular meshing avoids artefacts in the local field distributions at curved surfaces and thus provides a good representation of surface charge distributions, the FDTD with the light propagating in discrete time steps and measurement monitors provides a direct representation of the experiment.

b. Sample Fabrication High precision glass cover slides (Roth) with a thickness of $170 \pm 5 \mu\text{m}$ were used as transparent substrates. To obtain a conductive sample surface, a thin layer of indium tin oxide (ITO) was

deposited by sputter coating (AJA International Inc.). Thickness and complex refractive wavelength of the ITO layer were determined by ellipsometry measurements of a silicon reference chip covered in the same sputter run. The obtained ITO layer thickness was 30 nm with a weakly dispersive refractive index around 2.0 and negligible losses in the investigated wavelength range. The helices were fabricated by direct electron beam writing in a Thermo Fisher Helios 5 UX dual beam microscope using the metal-organic precursor Au(acac)Me₂ (dimethyl-(acetylacetone)gold(III)). The precursor reservoir is heated to 30 °C to mobilize and locally deliver the gas molecules by an injection nozzle. The molecules physisorbed at the surface are then decomposed by the focused electron beam with the non-volatile part forming the deposit while the volatile rest is pumped out.

c. Optical Measurements The optical characterization was carried out using a confocal transmission spectroscopy setup in the wavelength range between 500–800 nm. Circularly polarized light from a supercontinuum laser (FIR-20, NKT Photonics) in combination with spectral filter (VIS HP8, NKT Photonics) was focused onto the backside of the sample to a waist diameter of approximately 1 μm for all wavelengths. The transmitted signal was collected using a photodiode (S120C, Thorlabs) connected to an optical power meter (PM5020, Thorlabs) and normalized using the background signal from the area next to the double helix as a reference for each wavelength.

More details on modeling, fabrication and characterization of the double helical antennas can be found in the Supporting Information.

ACKNOWLEDGMENTS

The authors would like to thank Sabrina Jürgensen and Stephanie Reich for fruitful discussions about optical characterization, Victor Deinhart for the help with the pattern generation, and Lorentz Löfller for fruitful discussion regarding the theoretical model improvement.

FUNDING INFORMATION

This work was funded by the Deutsche Forschungsgemeinschaft (DFG, German Research Foundation) under Project ID HO5461/3-1 “chiralFEBID.” and by the Swiss National Fund by the COST – SNF project IZCOZ0_205450. The authors want to furthermore acknowledge financial support by the EU COST action CA 19140 ‘FIT4NANO’ (www.fit4nano.eu).

[1] G. Moody, V. J. Sorger, D. J. Blumenthal, P. W. Juodawlkis, W. Loh, C. Sorace-Agaskar, A. E. Jones,

K. C. Balram, J. C. F. Matthews, A. Laing, M. Davanco, L. Chang, J. E. Bowers, N. Quack, C. Gal-

- land, I. Aharonovich, M. A. Wolff, C. Schuck, N. Sinclair, M. Lončar, T. Komljenovic, D. Weld, S. Mookherjea, S. Buckley, M. Radulaski, S. Reitzenstein, B. Pingault, B. Machielse, D. Mukhopadhyay, A. Akimov, A. Zheltikov, G. S. Agarwal, K. Srinivasan, J. Lu, H. X. Tang, W. Jiang, T. P. McKenna, A. H. Safavi-Naeini, S. Steinhauer, A. W. Elshaari, V. Zwiller, P. S. Davids, N. Martinez, M. Gehl, J. Chiaverini, K. K. Mehta, J. Romero, N. B. Lingaraju, A. M. Weiner, D. Peace, R. Cernansky, M. Lobino, E. Diamanti, L. T. Vidarte, and R. M. Camacho, 2022 roadmap on integrated quantum photonics, *Journal of Physics: Photonics* **4**, 012501 (2022).
- [2] E. M. Purcell, Spontaneous emission probabilities at radio frequencies, *Phys. Rev.* **69**, 681 (1946).
- [3] K. J. Vahala, Optical microcavities, *nature* **424**, 839 (2003).
- [4] P. Biagioni, J.-S. Huang, and B. Hecht, Nanoantennas for visible and infrared radiation, *Reports on Progress in Physics* **75**, 024402 (2012).
- [5] A. F. Koenderink, Single-photon nanoantennas, *ACS Photonics* **4**, 710 (2017).
- [6] S. A. Maier *et al.*, *Plasmonics: fundamentals and applications*, Vol. 1 (Springer, 2007).
- [7] D. N. Basov, M. M. Fogler, and F. J. G. de Abajo, Polaritons in van der waals materials, *Science* **354**, aag1992 (2016).
- [8] T. Feichtner, S. Christiansen, and B. Hecht, Mode Matching for Optical Antennas, *Phys. Rev. Lett.* **119**, 217401 (2017).
- [9] T. H. Taminiau, F. D. Stefani, F. B. Segerink, and N. F. V. A. N. Hulst, Optical antennas direct single-molecule emission, *Nat. Phot.* **2**, 234 (2008).
- [10] M. Hentschel, M. Schäferling, X. Duan, H. Giessen, and N. Liu, Chiral plasmonics, *Science Advances* **3**, 1 (2017).
- [11] I. Fernandez-Corbaton, M. Fruhnert, and C. Rockstuhl, Objects of maximum electromagnetic chirality, *Physical Review X* **6**, 031013 (2016).
- [12] I. Fernandez-Corbaton, R. Griesmaier, M. Knöller, and C. Rockstuhl, Maximizing the electromagnetic chirality of thin metallic nanowires at optical frequencies, *Journal of Computational Physics* **475**, 111854 (2023).
- [13] F. Flamini, N. Spagnolo, and F. Sciarrino, Photonic quantum information processing: a review, *Reports on Progress in Physics* **82**, 016001 (2018).
- [14] C. A. Balanis, *Antenna theory: analysis and design* (John wiley & sons, 2016).
- [15] P. Woźniak, I. De Leon, K. Höflich, C. Haverkamp, S. Christiansen, G. Leuchs, and P. Banzer, Chiroptical response of a single plasmonic nanohelix, *Optics express* **26**, 19275 (2018).
- [16] K. Höflich, T. Feichtner, E. Hansjürgen, C. Haverkamp, H. Kollmann, C. Lienau, and M. Silies, Resonant behavior of a single plasmonic helix, *Optica* **6**, 1098 (2019).
- [17] L. Kuen, S. Burger, L. Zschiedrich, and T. Feichtner, Chiral and directional optical emission from a dipole source coupled to a helical plasmonic antenna, *Appl. Phys. Lett.* **124**, 231102 (2024).
- [18] M. Wang, R. Salut, H. Lu, M.-A. Suarez, N. Martin, and T. Grosjean, Subwavelength polarization optics via individual and coupled helical traveling-wave nanoantennas, *Light: Science & Applications* **8**, 76 (2019).
- [19] M. Wang, Z. Huang, R. Salut, M. A. Suarez, H. Lu, N. Martin, and T. Grosjean, Plasmonic helical nanoantenna as a converter between longitudinal fields and circularly polarized waves, *Nano Letters* **21**, 3410 (2021).
- [20] E. Prodan, C. Radloff, N. J. Halas, and P. Nordlander, A hybridization model for the plasmon response of complex nanostructures, *Science* **302**, 419 (2003).
- [21] Commonly referred as the antibonding and bonding modes in analogy to chemical terminology.
- [22] A. Moradi, Plasmon hybridization in parallel nano-wire systems, *Physics of Plasmas* **18**, 064508 (2011), publisher: American Institute of Physics.
- [23] E. Hecht, *Optik – 4., überarbeitete Auflage* (Oldenbourg Wissenschaftsverlag, 2005).
- [24] L. Novotny, Effective wavelength scaling for optical antennas, *Phys. Rev. Lett.* **98**, 266802 (2007).
- [25] Python scripts for the analytical calculations and the design tool are available under: <https://sourceforge.net/projects/plasmonic-helix-1dmodel/>.
- [26] C. F. Bohren and D. R. Huffman, *Absorption and Scattering of Light by Small Particles* (John Wiley & Sons, 1983).
- [27] P. B. Johnson and R.-W. Christy, Optical constants of the noble metals, *Physical review B* **6**, 4370 (1972).
- [28] I. Utke, P. Hoffmann, and J. Melngailis, Gas-assisted focused electron beam and ion beam processing and fabrication, *Journal of Vacuum Science & Technology B: Microelectronics and Nanometer Structures Processing, Measurement, and Phenomena* **26**, 1197 (2008).
- [29] K. Höflich, R. B. Yang, A. Berger, G. Leuchs, and S. Christiansen, The direct writing of plasmonic gold nanostructures by electron-beam-induced deposition, *Advanced materials* **23**, 2657 (2011).
- [30] C. Haverkamp, K. Höflich, S. Jäckle, A. Manzoni, and S. Christiansen, Plasmonic gold helices for the visible range fabricated by oxygen plasma purification of electron beam induced deposits, *Nanotechnology* **28**, 055303 (2016).
- [31] M. Esmann, S. C. Wein, and C. Antón-Solanas, Solid-state single-photon sources: Recent advances for novel quantum materials, *Advanced Functional Materials* **n/a**, 2315936 (2024).
- [32] M. Esposito, V. Tasco, M. Cuscunà, F. Todisco, A. Benedetti, I. Tarantini, M. D. Giorgi, D. Sanvitto, and A. Passaseo, Nanoscale 3d chiral plasmonic helices with circular dichroism at visible frequencies, *ACS Photonics* **2**, 105 (2015).
- [33] J. Kaschke, L. Blume, L. Wu, M. Thiel, K. Bade, Z. Yang, and M. Wegener, A helical metamaterial for broadband circular polarization conversion, *Advanced Optical Materials* **3**, 1411 (2015).
- [34] V. Deinhart, L.-M. Kern, J. N. Kirchhof, S. Juergensen, J. Sturm, E. Krauss, T. Feichtner, S. Kovalchuk, M. Schneider, D. Engel, B. Pfau, B. Hecht, K. I. Bolotin, S. Reich, and K. Höflich, The patterning toolbox fibomat: Exploiting the full potential of focused helium ions for nanofabrication, *Beilstein Journal of Nanotechnology* **12**, 304 (2021).
- [35] L. Keller and M. Huth, Pattern generation for direct-write three-dimensional nanoscale structures via focused electron beam induced deposition, *Beilstein Journal of Nanotechnology* **9**, 2581 (2018).
- [36] A. Szkudlarek, W. Szmyt, C. Kapusta, and I. Utke, Lateral resolution in focused electron beam-induced deposition: scaling laws for pulsed and static exposure, *Applied Physics A* **117**, 1715 (2014).

- [37] J. D. Fowlkes, R. Winkler, B. B. Lewis, A. Fernandez-Pacheco, L. Skoric, D. Sanz-Hernandez, M. G. Stanford, E. Mutunga, P. D. Rack, and H. Plank, High-fidelity 3d-nanoprinting via focused electron beams: computer-aided design (3bid), *ACS Applied Nano Materials* **1**, 1028 (2018).
- [38] I. Utke, A. Luisier, P. Hoffmann, D. Laub, and P. Buffat, Focused-electron-beam-induced deposition of freestanding three-dimensional nanostructures of pure coalesced copper crystals, *Applied Physics Letters* **81**, 3245 (2002).
- [39] E. Mutunga, R. Winkler, J. Sattelkow, P. D. Rack, H. Plank, and J. D. Fowlkes, Impact of electron-beam heating during 3d nanoprinting, *ACS nano* **13**, 5198 (2019).
- [40] N. Silvis-Cividjian, C. Hagen, L. Leunissen, and P. Kruit, The role of secondary electrons in electron-beam-induced-deposition spatial resolution, *Microelectronic engineering* **61**, 693 (2002).

Appendix A: Numerical Modeling

As described in the main manuscript full-field modeling was carried out using commercial Maxwell solvers. Two different modeling techniques were employed. The scenario without substrate corresponding to the described case in the semi-analytical model was modeled using the finite element method (FEM). The scenario with substrate was modeled using a finite-difference time-domain (FDTD) technique. In FEM (COMSOL Multiphysics) the helix geometry and plane wave illumination was implemented into a full-field scattered-field environment terminated by perfectly matched layers (PML). The normal component of the dielectric displacement with respect to the helix surfaces was used to visualize the surface charge distribution. FDTD modeling (Ansys Lumerical FDTD) of the same geometry and using the same material parameters proved that the substrate influence is negligible for the aspect ratio of this geometry. Accordingly, g_{num} was obtained by modeling the transmission of LCP and RCP through the right-handed double helix with FDTD method and calculated by using the same formula as for g_{exp} . The intensities of total and scattered field were obtained by projecting the corresponding Poynting vectors onto a surrounding integration surface and used to obtain the scattered and absorbed (total - scattered) intensities. The antenna geometry consist of two helices with a relative rotation of 180° with respect to each other. The helices have $m = 4$ turns with a helix pitch λ_h of 430 nm, a helix radius r_h of 100 nm and a wire radius r_w of 32 nm with the wires being terminated with round caps of the same radius. The permittivity of gold was defined using an analytical fit function to the data of Johnson and Christie [27] in both cases. It should be noted that the models do not take into account the thickness of the gold shell and random gold particles that are scattered at the base of the helix. These particles are randomly deposited with secondary and scattered electrons and become visible after cleaning with oxygen plasma.

In the following additional plots of the spectral response are provided.

Figure SI1 displays the same data as Figure 2(c) in the main manuscript but plotted over the energy. Here, the Fabry-Perot modes from the semi-analytical model appear equally spaced. Still, a pronounced shift due to plasmon hybridization at the double wires is only visible in the low-energy region. The resonance broadening for the higher order (higher energy) modes is generally larger than that for the lower order modes. Therefore, the high-order modes are not spectrally resolvable in the energy scale either.

Figure SI2 disentangles the contributions scattering and absorption to the total extinction. While the two modes discussed in the main manuscript ($n = 6$ and $n = 14$) are mainly scattering, the sharp $n = 5$ mode is mostly absorbing.

Radiation patterns of the free standing double helix as a scatterer are shown in Figure SI3 of the main

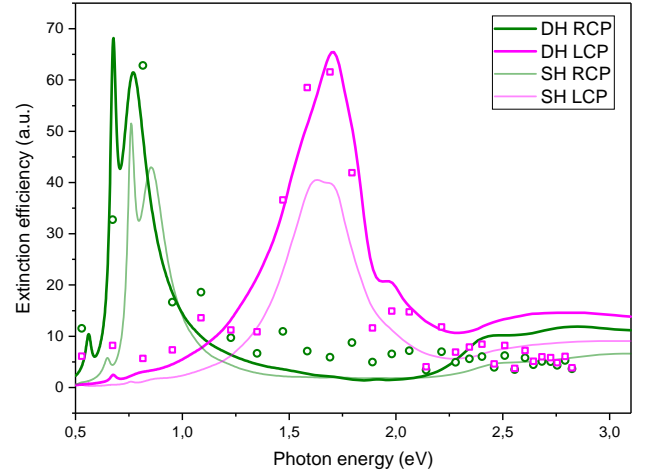


FIG. SI1. FEM simulation results on total extinction efficiency for the double helix plotted vs. photon energy, investigated in the main manuscript.

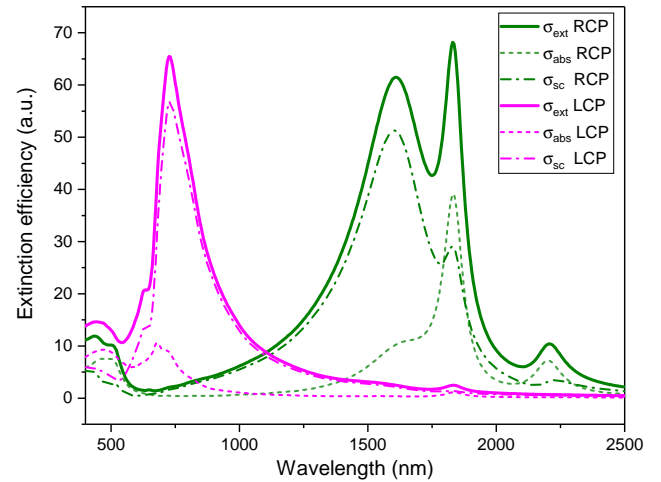


FIG. SI2. FEM simulation results on total scattering and absorption for the double helix, investigated in the main manuscript.

manuscript, for left circularly polarized light at 725 nm and for right circularly polarized light at 1830 nm. In both cases, the double helix exhibits strongly directional scattering characteristics, with the maximum energy scattered within approximately 60° . Interestingly, the radiation pattern at 725 nm is exceptionally asymmetric, with the scattered light propagating along the helical axis in the same direction as the incident light. This can be explained by the fact that the wavelength is almost twice as short as the height of the helix, which results in retardation effects and excitation of several neighboring modes. This is diminished at 1610 and 1830 nm, at which helix scatters some radiation backwards.

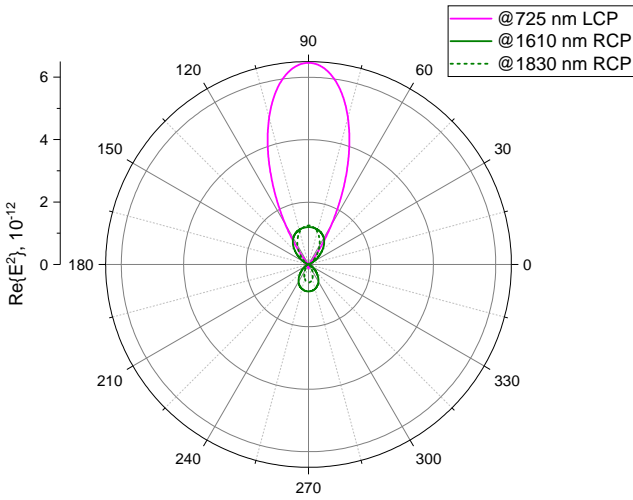


FIG. SI3. Radiation pattern based on FDTD simulation results on scattering of the double helix at 725 nm LCP and 1610 and 1830 nm RCP in the far-field.

Appendix B: Fabrication Strategy and Material Analysis

Double helices were fabricated by direct electron beam writing i.e. the local dissociation of gaseous precursor molecules by focused electron beam impact. The metal-organic compound dimethyl(acetylacetone)gold(III), short: Au(acac)₂Me₂ (CAS no. 14951-50-9) was employed as a precursor. It was heated to 30°C in side gas injection system with then gaseous molecules injected into a vacuum chamber. The electron beam locally dissociates the physisorbed molecules, forming a deposit from non-volatile parts after decomposition. The base background pressure before deposition was 5.3·10⁻⁷ mbar. Upon opening the nozzle valve, the background pressure stabilized at 5.8·10⁻⁷ mbar. Deposition was started few minutes later after recovering the pressure close to the initial value to ensure for uniform precursor delivery over time.

Figure SI4(a) depicts the star-shaped electron beam path for the parallel printing of the both helix arms, created with Python toolbox Fib-o-Mat [34]. The electron beam starts at point 1 for the first helix for a certain dwell time and then jumps to point 2 for the second helix. After the same dwell time beam jumps back to point 3 on the first helix, which is slightly shifted along circumference counter-clockwise. This step is then repeated many times to form the double helix. The corresponding SE micrograph of the resulting helix right after deposition is displayed in Figure SI4(b). The beam path parameters to be optimized are the pitch (distance between two neighboring points) and dwell time, as these determine the beam velocity and thus the vertical growth rate. Here, the beam path combines two timescales. The longer times define the beam velocity for deposition in tangential direction and on a short time scale the ra-

dial movement provides for parallel printing. The latter jumping from helix to helix also assists in precursor refreshment[35]. The radial movement should be fast enough to avoid unwanted deposition within the helical geometry. The local precursor supply is mainly driven by diffusion [28, 36, 37] what impedes spurious deposition inside of the helical geometry. Furthermore, the wire-like geometries thermally decouple from the substrate with increasing height [38]. Correspondingly, the energy input by the electron beam increases the local temperatures onto the deposit surface which in turn decreases the molecule residence times [39]. Both effects decrease molecule density for increasing structure height shifting the deposition into the mass-transport-limited regime. The resulting pronounced decrease in the vertical growth rate was compensated by a dynamic increase of the dwell times. Apart from this, many more physical parameters are important. The electron beam current adjusts the number of available electrons in the focus. In the reaction-rate limited growth regime an increased current leads to an increase of both, wire diameter and vertical growth rate. However, since our geometries eventually enter the mass-transport-limited regime as detailed above, small beam currents (approximately 100 pA) are preferred to keep the local precursor replenishment as constant as possible [35]. The primary energy of the electrons determines the size of the collision cascade, which is related to the yield and spatial distribution of secondary electrons that drive the process [40]. High beam energies above 15 keV, while beneficial in allowing the smallest electron beam spots and the sharpest deposition features, result in elongation of the wire form that is more pronounced the more horizontal they are [37]. In this work, the beam energies were therefore reduced to 5 kV resulting in a relatively round wire shape. In addition, the position of focal plane drastically affects the vertical growth rate as well as wire thickness and had to be fixed above the sample surface by an auxiliary deposit for focusing. The minimum achievable dimensions of the double helix are not given by the wire thickness, but by the attractive Coulomb forces. As soon as the helix arms are too close together, the continuous supply of electrons during writing causes them to approach and eventually touch.

In case of the used dimethyl(acetylacetone)gold(III) compound the resulting deposit consists of single-crystalline gold particles embedded in a carbonaceous matrix [29]. To achieve the desired material response, a pure metal surface has to be realized with a thickness exceeding the skin depth in the relevant spectral range. As-deposited helices were purified in Zepto Diener oxygen plasma cleaner for 60 sec with 0.2 sccm oxygen flux which roughly corresponds to less than 0.3 mbar background pressure to obtain closed pure gold shell. After purification the surface appears roughened as shown in the scanning electron micrograph of Figure SI4(c).

If the wire diameter is too thin, plasma cleaning leads to a slight bending of the helix arms, which can eventu-

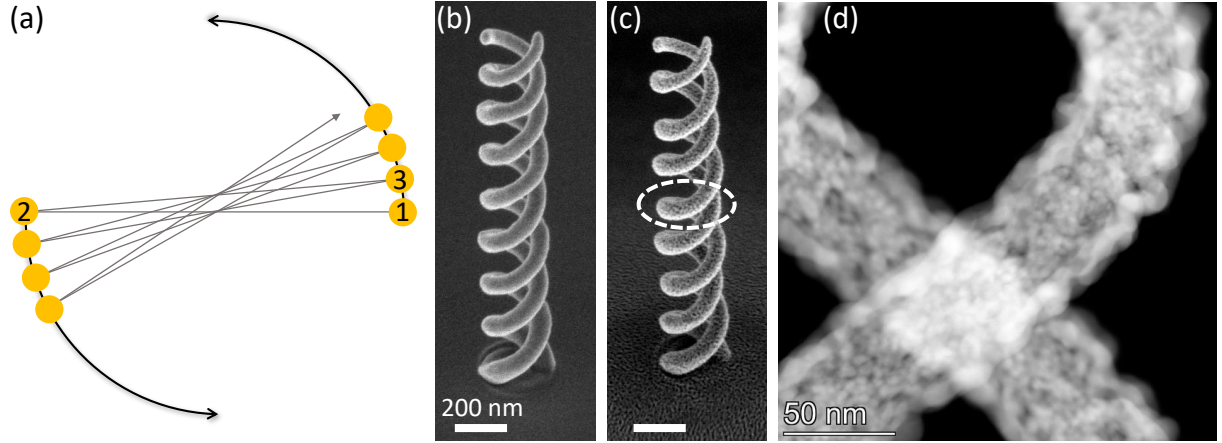


FIG. SI4. (a) Star-shaped pattern for parallel deposition of both arms of the double helix. (b) SE micrograph of the as-deposited double helix made from Au, 45° side view. (c) SE micrograph of the double helix after oxygen plasma cleaning, 45° side view. (d) STEM HAADF image of double helix after purification depicting the presence of gold shell.

ally destroy the helix. This sets a lower limit for the wire thickness of 60 nm.

After purification the helices were characterized with a probe-corrected ThermoFisher Scientific Titan Themis 200 G3 TEM for their microstructure and composition. Figure SI4(d) show a high-angle annular dark-field (HAADF) image of the two helix arms after purification in which the agglomerated particles at the surface form a thin layer. After 1 min treatment in oxygen plasma approximately 15 nm of outer shell on the helix was purified and consists of almost perfectly closed gold shell. The core of the helix resembles the typical compound multi-crystalline gold structure, embedded in carbon.

Appendix C: Optical Measurements

Fabricated samples were optically characterized in a transmission setup shown in Figure SI5. As an excitation source we used super-continuum laser (FIR-20, NKT Photonics) in combination with spectral filter (VIS HP8, NKT Photonics) producing narrow spectral lines of width less than 2.5 nm, in the spectral range from 500 to 800 nm. Laser light was focused onto the substrate to a spot with a diameter of approximately 1 μm using 60x magnification objective with high numerical aperture (0.95 NA, CFI Plan Apo Lambda 60XC, Nikon). In the detection path the backlens of the objective was only partially filled. RCP and LCP light was generated by combination of linear polarizer and achromatic quarter-wave plate (AQWP10M-980, Thorlabs). Scattered light together with primary excitation beam passing through a double helix was then collected using long working-distance objective, with 100x magnification and 0.7 NA (MY100X-806, Mitutoyo), and directed to a photodiode (S120C, Thorlabs) connected to an optical power meter (PM5020, Thorlabs).

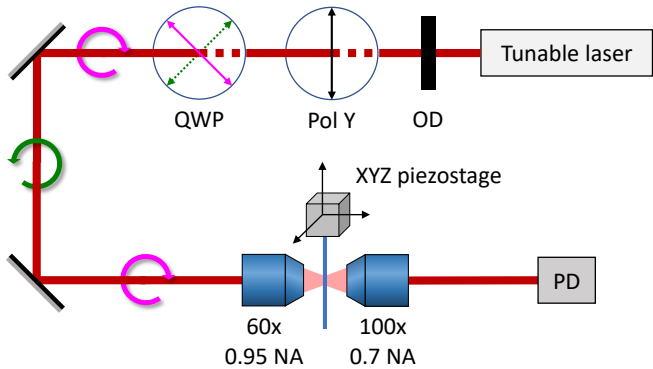


FIG. SI5. Sketch of the transmission confocal microscopy setup.